Article

Effects of Process Parameters on Bond Properties of Ag-2.35Au-0.7Pd-0.2Pt-0.1Cu Alloy Wire

Hongliang Zhou[1],*, Andong Chang[1], Jun Cao[1],*, Yingchong Zhang[1,2], Bin An[1] and Jie Xia[1]

[1] School of Mechanical and Power Engineering, Henan Polytechnic University, Jiaozuo 454000, China; zhl-hpu@hpu.edu.cn; cavan@hpu.edu.cn

[2] Nanjing High Speed Gear Manufacturing Co., Ltd., Nanjing 211100, China; 212005010007@home.hpu.edu.cn

* Correspondence: zhlhpu@hpu.edu.cn; cavan@hpu.edu.cn

Abstract: Bond Properties were performed on Ag-2.35Au-0.7Pd-0.2Pt-0.1Cu alloy wire with a diameter of 25 µm under different process parameters. Effects of electrical flaming off (EFO) current and EFO time on deformability of the free air ball (FAB) were investigated using scanning electron microscopy (SEM) as well as the effects of ultrasonic power and bonding force on the bond characteristic. The experimental results showed that, FAB grows from a preheated tip to a small ball, a regular ball and finally to a golf ball with increasing either the EFO current or the EFO time, and the FAB presented optimal shape at 25 mA and 650 µs. Moreover, a nonlinear relationship between FAB diameter and EFO time is obtained at the EFO current of 25 mA, which could be expressed by a cubic equation. Further, at a constant bonding force, as the ultrasonic power increased, the mashed ball diameter grew larger and larger, the capillary hole imprint became more and more obvious, and the tail width also increased larger and larger, and vice versa. The optimal ultrasonic power and bonding force are 70 mW and of 45 gf for ball bond and 90 mW and 75 gf for wedge bond, respectively. Finally, for all the bonded wire samples prepared under optimal process parameters, no ball and wedge bond lifts happened after destructive pull test, and full intermetallic compound coverage with perfect morphology occurred on the bond pad after ball shear test, which meant that the bonded wire samples have high bond strength, and hence improved the reliability of microelectronic products.

Keywords: bond properties; EFO current; EFO time; ultrasonic power; bonding force

1. Introduction

Microelectronics packaging is an overarching part of the microelectronics industry, which is one of the main pillar industries in the world. Microelectronic products have been extensively used in all fields of social life, and is driving the continuous development and technology innovation of the overall electronic industry, whose quality and lifespan are influenced by microelectronic packaging technology [1]. Wire bonding is the most common technique for forming electrical interconnections in the microelectronics industry because of its cost-effectiveness, flexibility and robustness, which forms the primary semiconductor packages in the field of microelectronic packaging currently [2-4]. The bonding wire, an essential structural material for microelectronic packaging, plays a significant role in connecting the integrated circuit (IC) chips to the metal lead frame [5].

Au bonding wire, as the earliest and most widely used bonding wire, has excellent mechanical and electrical properties, high reliability, and ease of assembly. However, due to the increasingly high cost of Au and its limited performance development in recent years, alternative bonding wires have been considered [6-9]. Cu bonding wire is a preferred alternative material because of its lower cost, slower intermetallic growth on Al pads, and higher thermal conductivity and mechanical strength compared with Au bonding wire [10-12], while researchers agree that Cu bonding wire is not the definitive substitute for Au bonding wire due to its high hardness and oxidation rate and complex

bonding process that will result in damage of pad during bond [13-15]. Ag bonding wire, as a promising material for the development trend of microelectronic packaging with high density, high integration, and high speed, has lower cost, better manufacturability, and higher reliability than Au and Cu bonding wires [16-18], and it has been utilized in integrated circuit (IC) and light-emitting diode (LED) packaging [19-21].

However, pure Ag wire has some problems such as easy oxidation, easy collapse, and Ag+ migration that make it applied inconveniently, the alloying can solve the above problems and provide an effective way to develop new Ag bonding wires of low cost and high reliability [22]. Fan et al [23] studied the bond strength and reliability of Ag-Au alloy wires with different Au contents (1wt%, 3wt%, 5wt%), and found that with the increases of Au content, the size of heat-affected zone (HAZ) decreases, the tension and shearing force of the free air ball (FAB) increase, and when the Au content is 5wt%, the best FAB morphology can be got. Ag alloy wires with various contents of Pd and Au were evaluated by Tsai et al., the experimental results presented that their breaking load increases with Au and Pd contents [24]. Cao et al. [25] made a study on the effect of annealing temperature on the properties of Ag-8.5Au-3.5Pd alloy wire, and the results revealed that the alloy wire has good mechanical properties at 500 ℃. Chuang et al. [26, 27] provided that an innovative Ag-8Au-3Pd alloy wire with a high twin density can be produced through appropriate drawing and annealing processes, which exhibits high thermal stability during high temperature exposure.

The above-described studies are mostly performed on the performance of Ag alloy wires with Au and Pd elements, in the present study, a new type of Ag alloy wire, named Ag-2.35Au-0.7Pd-0.2Pt-0.1Cu alloy (AAPPCA) wire, is obtained by further adding Pt and Cu elements to triple Ag-Au-Pd alloy, whose FAB morphology and bond strength were studied, and then the optimal electrical flaming off (EFO) and bonding parameters for the AAPPCA wire were obtained. Hopefully, the results of this study could serve as the academic and theoretical basis for the use of AAPPCA wire in microelectronic packaging.
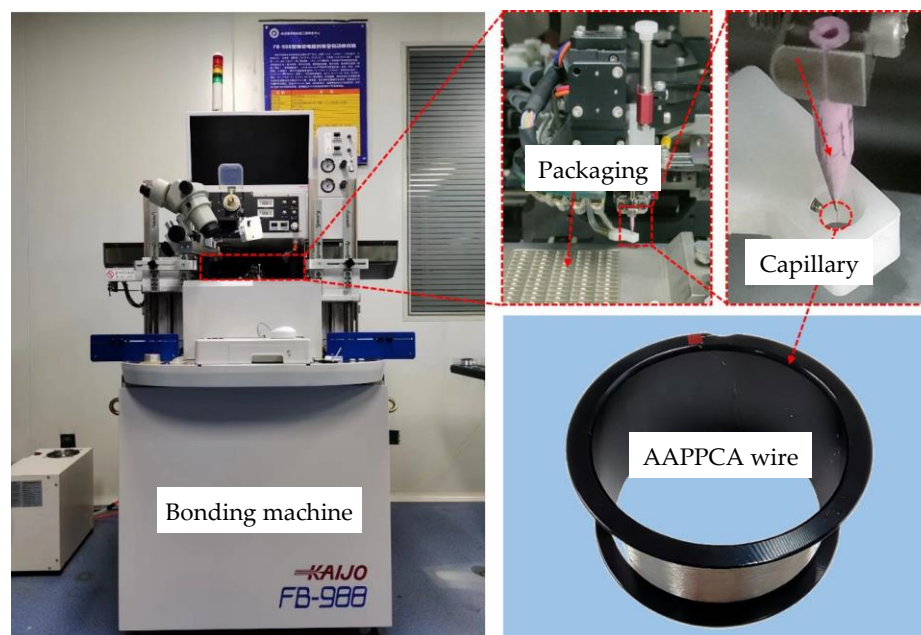

Figure 1. Experimental equipment and materials.

2. Materials and Methods

A KAIJO FB-988 automatic bonding machine made in Japan was employed in this study. The packaging type 2835 LED and capillary type SPT SU-50140-425E-ZU36-E were used, and an AAPPCA wire with a diameter of 25 μm was also employed here, whose average elongation and tensile strength are 11.5% and 259.1 MPa, respectively, as shown in Figure 1. N2 with a flow rate of 0.6L/min was used as a shielding gas to prevent the oxidation of the molten AAPPCA wire during EFO process,

and the process parameters are shown in Table 1. The morphology of FAB and bonds was observed using a scanning electron microscope (SEM) system, and the relationship between FAB diameter and EFO time was fitted. The bond strength was measured using a DAGE Series 4000 BS250 system at a test speed of 500 μm/s and shear height of 5 μm.

Table 1. Process parameters for AAPPCA wire

| Free Air Ball		Ball Bond		Wedge Bond	
Spark Voltage/V	5000	Impact Force F_f/gf	65	Bonding Force F_1/gf	55
EFO Current/mA	20/25/30	Bonding Force F/gf	35/45/55	Ultrasonic Power P_1/mW	60
EFO Time/μs	500/550/600/650/ 700/750/800	Ultrasonic Power P/mW	60/70/80	Bonding Time t_1/ms	6
Tail Length/mm	0.15	Bonding Time t/ms	8	Bonding Force F_2/gf	55/75/95
Bonding Temperature/℃	220			Ultrasonic Power P_2/mW	80/90/100
				Bonding Time t_2/ms	6
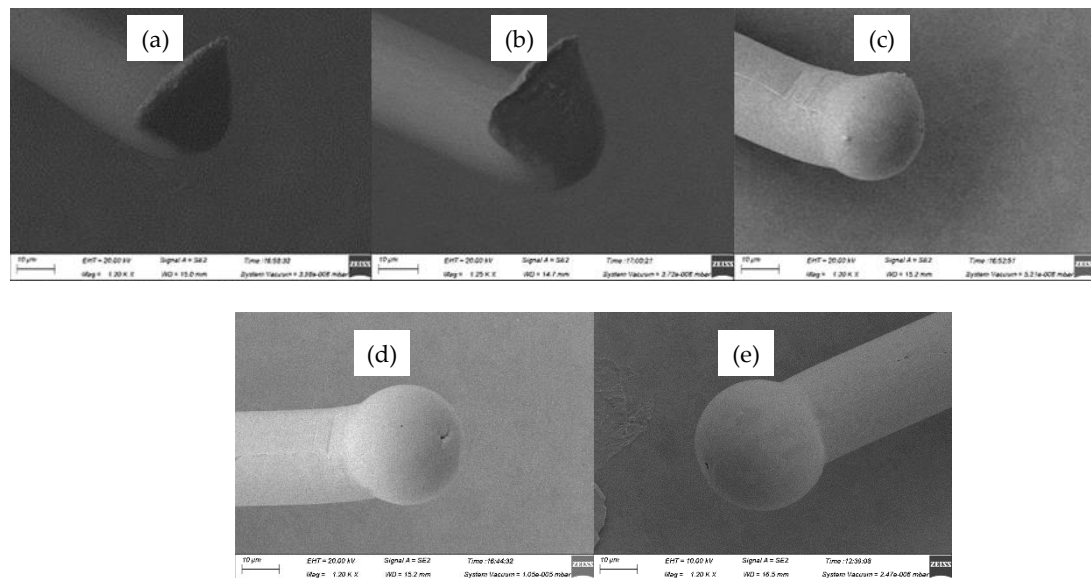
Figure 2. FAB morphologies of AAPPCA wire for different EFO times at 20 mA: (a) 550 μs, (b) 600 μs, (c) 650 μs, (d) 700 μs, (e) 750 μs

3. Results and Discussions

3.1. Effects of EFO Current and EFO Time on FAB Morphology of AAPPCA wire

During the EFO process, inappropriate EFO parameters will result in FAB with imperfect morphology and sphericity, and then obviously cause poor ball bonding contact, which has a bad effect on the bonding yield. It is closely related to the solidification process during FAB formation, so optimal EFO parameters should be chosen carefully.

Figure 2 showed the FAB morphologies of AAPPCA wire for different EFO times at a constant EFO current of 20 mA. It could be seen that the wire tip is preheated by the EFO discharge from 550 μs to 600 μs, as shown in Figures 2a-b. When the EFO time increases from 550 μs to 750 μs, the bonding wire has a small FAB with poor sphericity, since the EFO current of 20 mA generates inadequate energy to melt the wire tail, which results in the smaller FAB than a standard one even under the effect of surface tension. What is worse, a hollow is found at the bottom of FAB due to a lack of energy

input via arc discharging, as shown in Figures 2c-e, which is unacceptable in practical applications. It indicated that a higher EFO current than 20 mA is needed to form a standard FAB of the AAPPCA wire to satisfy the bonding yield.

Figure 3 showed the FAB morphologies of AAPPCA wire for different EFO times at a constant EFO current of 25 Ma. It was found that the FAB diameter at 25 Ma is larger than that at 20 Ma, for the reason that higher EFO current of 25 Ma generated enough energy to melt the wire tail completely. At 550-650 μs, a regular FAB with smooth surface solidify from its neck to its bottom until it achieves the equilibrium position, as shown in Figures 3a-c. While at 700-750 μs, the off-center FAB can be observed from the AAPPCA wire, as shown in Figures 3d-e. A possible reason was that the spark from the EFO electrode reaches the wire on the side, which make the wire tail experience lower surface temperature on the opposite side, and thus the molten wire will lean to the spark side due to unbalanced surface tension on the two sides. Finally, a golf-clubbed FAB occurs after natural cooling that will result in misplacement of bond, weak bond or bond lift, and therefore worsen the bond strength and reliability.
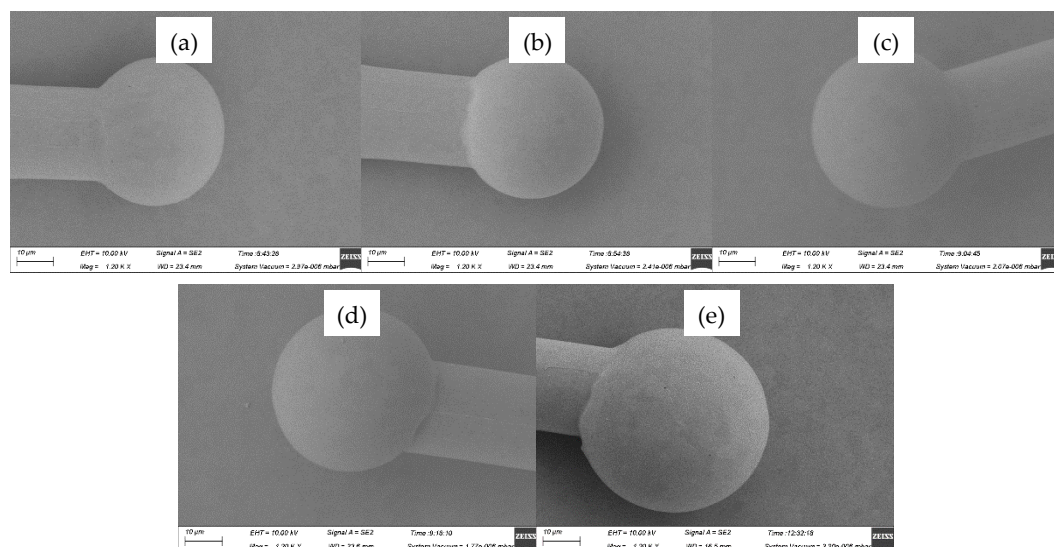

Figure 3. FAB morphologies of AAPPCA wire for different EFO times at 25 mA: (a) 550 μs, (b) 600 μs, (c) 650 μs, (d) 700 μs, (e) 750 μs

When the EFO current turned to 30 mA, the FAB forms rapidly because of a great amount of heat due to the large current, which causes the FAB center to deviate from that of the AAPPCA wire. As a result, more golf-clubbed FAB comes out at 550-750 μs, as shown in Figure 4. In consequence, the short circuits probably occurs in fine pitch ball bonding, which can't be accepted.

Considering the occurrence of off-center FAB at the EFO time of 25 mA, 700 μs, ten FAB samples forming at 25 mA, 650 μs were chosen to make further morphologies observation by SEM system. The results showed that all the ten FAB samples have smooth surface without defects, and presents approximately consistent diameter with perfect sphericity. The average diameter of the ten FAB samples was about 45.5 μm, as shown in Figure 5, which was 1.82 times that of the AAPPCA wire and in line with production requirement. In conclusion, the optimal EFO current and time are 25 mA and 650 μs, respectively.
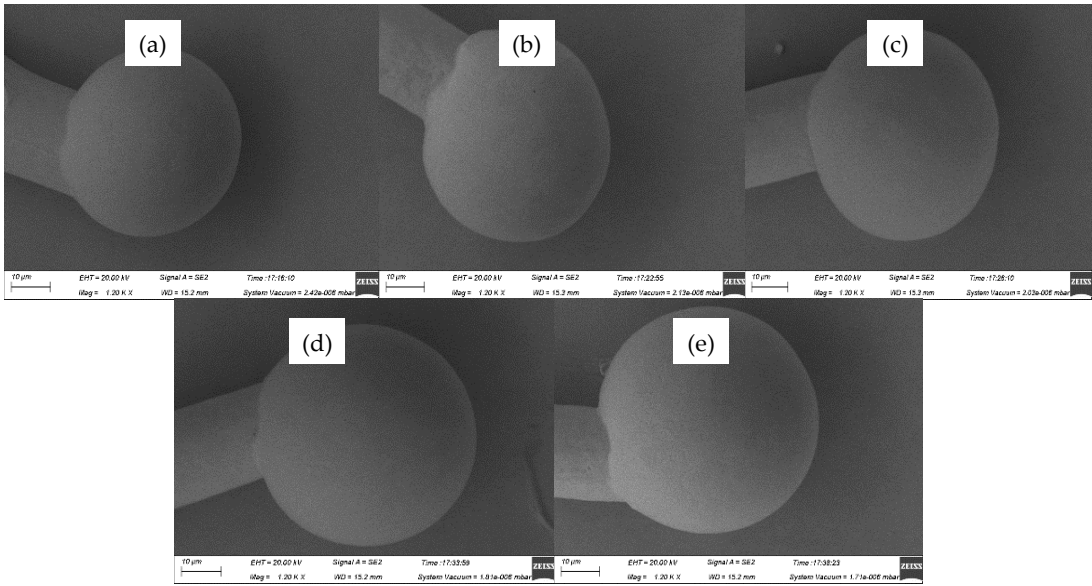
Figure 4. FAB morphologies of AAPPCA wire for different EFO times at 30 mA: (a) 550 μs, (b) 600 μs, (c) 650 μs, (d) 700 μs, (e) 750 μs
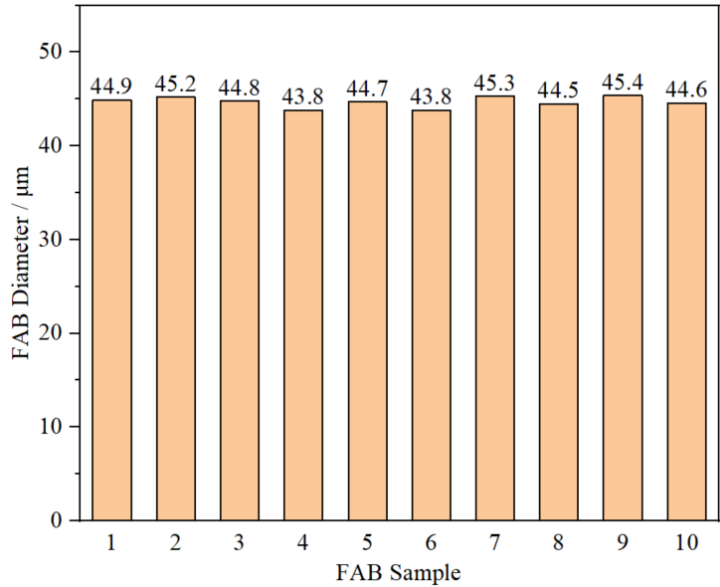

Figure 5. FAB diameter of the ten FAB samples forming at 25 mA, 650 μs

3.2. Relationship between FAB Diameter of AAPPCA wire and EFO Time

During the dynamic FAB formation process, EFO time is a key factor that dominants the FAB diameter at a constant EFO current, which affects the FAB growth rate and model. Generally, in the case of large die pad chips, a large FAB is appreciated that can give rise to a larger bond area and a higher bond strength. However, in the case of small die pad chips, too large FAB will result in molten metal spill and further short circuits [28].
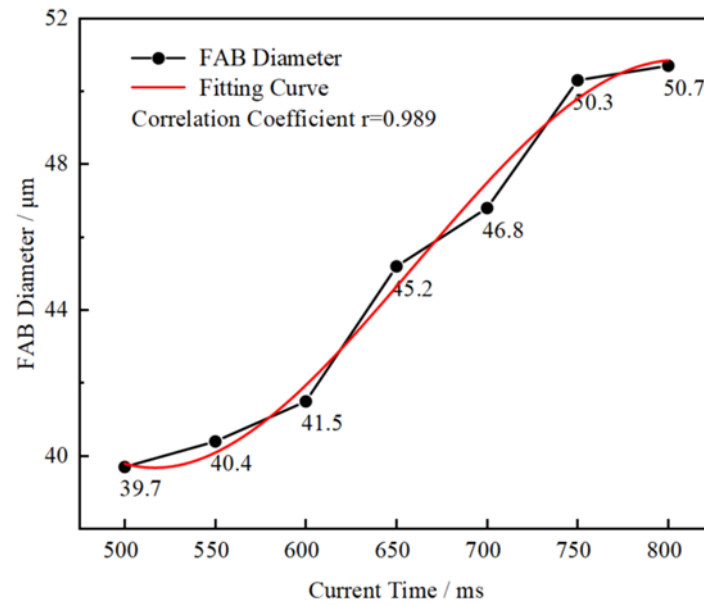
Figure 6. Relationship between the FAB diameter and EFO time of AAPPCA wire at the EFO current of 25 mA

The relationship between the FAB diameter and EFO time of AAPPCA wire at the EFO current of 25 mA was obtained by experiment, as shown in Figure 6, from which it could be seen that FAB diameter increases relatively quickly from 500 μs to 750 μs, while slowly after 750 μs. A cubic equation representing the relationship between the FAB diameter and EFO time was obtained by fitting the experimental data by using least square method.

$$d = -9.33327 \times 10^{-7} t^3 + 0.00185 t^2 - 1.16416t + 276.04126$$

Where d is the FAB diameter, t is the EFO time.

Further, the correlation coefficient, r of 0.989 was also obtained by the least square method with the confidence interval of 500-800 μs. It means that the above cubic equation can be used by microelectronics industry to determine the EFO time for AAPPCA wire with a diameter of 25 μm.

3.3. Effects of Ultrasonic Power and Bonding Force on Ball Bond Morphology of AAPPCA wire

Ultrasonic power and bonding force are key factors affecting bondability in the bonding process. The contamination and oxide layer can be broken down by ultrasonic vibration to improve the interfacial adhesion between FAB and pad metal. An ultrasound energy can lower the bonding force by softening FAB effectively, and then increases the dislocation density, thereby lowering the flow stress. The bonding force produces sliding friction at the interface, which leads to some wear and then to the bond being formed.

Figure 7 gave the SEM images of ball bands for various ultrasonic power, ranging from 60 mW to 80 mW, at a constant bonding force of 35 gf. The mashed balls in Figures 7a-c had relatively small diameters of 54.7 μm, 55.2 μm and 56.4 μm, respectively, due to the small bonding force of 35 gf, which would lead to low bond strength. What was worse, off-center ball bonds were also found in these cases, as shown in Figure 8, and thus had bad effects on bond quality.
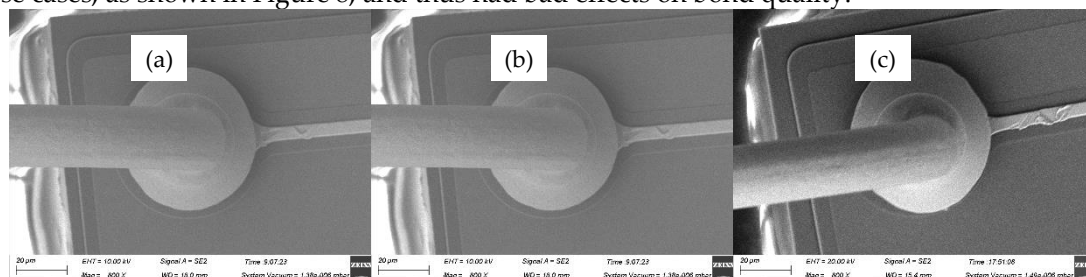

Figure 7. Ball bond morphologies of AAPPCA wire for different ultrasonic power at 35 gf: (a) 60 mW, (b) 70 mW, (c) 80 mW
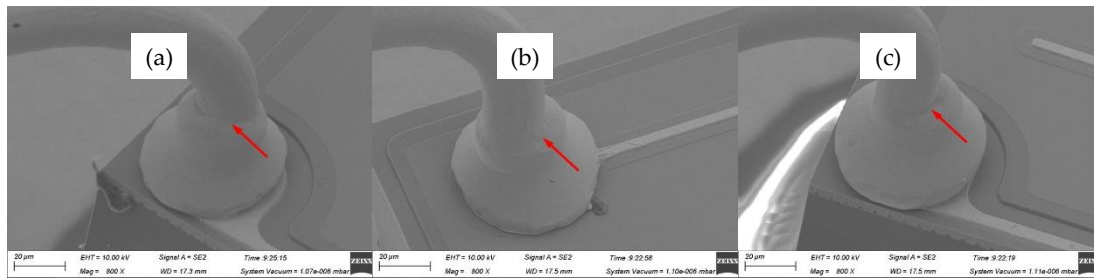
Figure 8. Off-center ball bond morphologies of AAPPCA wire for different ultrasonic power at 0.35 N: (a) 60 mW, (b) 70 mW, (c) 80 mW

Figure 9 presented the ball band morphologies for various ultrasonic power, ranging from 60 mW to 80 mW, at a constant bonding force of 45 gf. The mashed ball diameters in Figures 9a-c were 57.6 μm, 59.4 μm and 59.7 μm, respectively, all of which were larger than that in Figures 8a-c. It meant that larger bonding force can produce larger contact area between FAB and pad metal and therefore improve bond strength effectively. However, oval mashed ball occurred at 80 mW, whose diameter only increased by 0.3 μm compared with that at 70 mW, and it would cause poor bond strength.
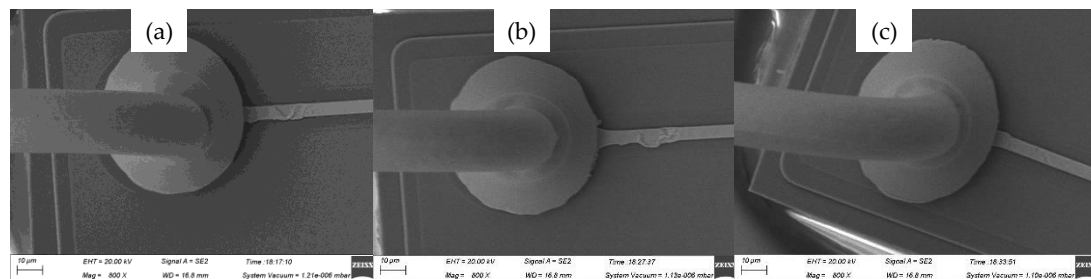

Figure 9. Ball bond morphologies of AAPPCA wire for different ultrasonic power at 45 gf: (a) 60 mW, (b) 70 mW, (c) 80 mW

When the bonding force was 55 gf, the ball band morphologies for various ultrasonic power, ranging from 60 mW to 80 mW, were shown in Figures 10a-c. It could be seen from Figure 10a that Al splash occurs at 60 mW because of the large bonding force of 55 gf, which would increase the risk of short circuit or circuit function disorder. Especially for the ball bonds shown in Figures10b-c, who formed at bond pad edge, large bonding force might cause cracking of the passivation at bond pad edge or might even lead to cracking of the substrate. Hence, the optimal ultrasonic power of 70 mW and bonding force of 45 gf were chosen here for the ball bond of AAPPCA wire in order to ensure ball bond reliability.
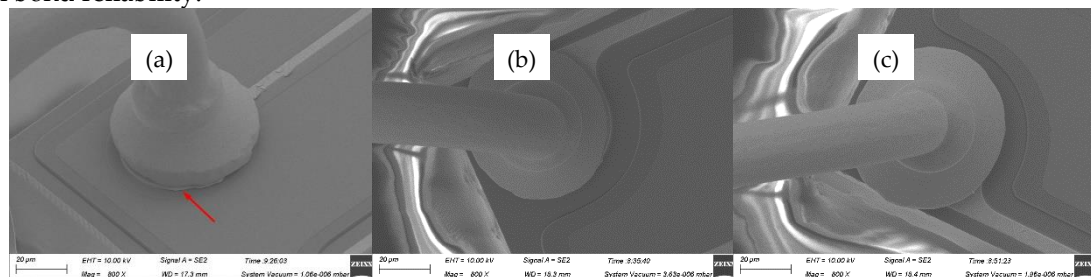

Figure 10.   Ball bond morphologies of AAPPCA wire for different ultrasonic power at 55 gf: (a) 60 mW, (b) 70 mW, (c) 80 mW

3.4. Effects of Ultrasonic Power and Bonding Force on Wedge Bond Morphology of AAPPCA wire

The wedge bond, also called stitch bond, is formed by the application of bonding force and ultrasonic energy by deformation of the wire between the capillary and the substrate or lead finger. Tail formation belongs to the last step in the bonding process as well as a necessary step to continue the bonding process. Stable wedge bond formation plays a significant role in stability of the thermosonic wire bonding process.

Figure 11 showed the wedge band morphologies for various ultrasonic power, ranging from 80 mW to 100 mW, at a constant bonding force of 55 gf. It could be found that the tail width increases with increasing the ultrasonic power. While, in Figure 11a, tail bond detached away from the substrate down to the inadequate ultrasonic power at 55 gf, which represented the bad bond quality and maximized production stoppages. No capillary hole imprint (CHI) in Figure 11b and indistinct one in Figure 11c were both indicated poor stitch bondability between wire and substrate, and posed risk in the long-term reliability.
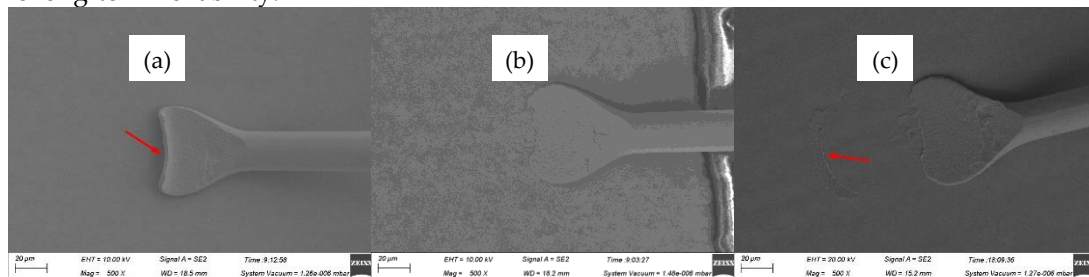

Figure 11. Wedge bond morphologies of AAPPCA wire for different ultrasonic power at 55 gf: (a) 80 mW, (b) 90 mW, (c) 100 mW
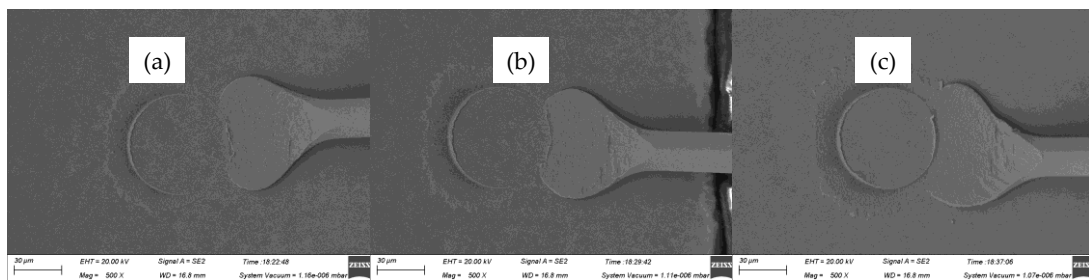

Figure 12. Wedge bond morphologies of AAPPCA wire for different ultrasonic power at 75 gf: (a) 80 mW, (b) 90 mW, (c) 100 mW

Figure 12 showed the wedge band morphologies for various ultrasonic power, ranging from 80 mW to 100 mW, at a constant bonding force of 75 gf. Compared with Figure 12a, Figure 13b exhibited more than half of CHI circle circumference and more symmetrical tail shape, which indicated that the wedge bond in Figure 12b has a higher bond strength than that in Figure 12a. While, Figure 12c showed complete CHI and asymmetric tail, which the wedge bond increased the risk of substrate damage and bond failure.

Figure 13 exhibited the wedge band morphologies for various ultrasonic power, ranging from 80 mW to 100 mW, at a constant bonding force of 95 gf. In such case, complete CHI could be found due to the large bonding force, who became more and more obvious with increasing ultrasonic power. What was worse, more asymmetric tails occurred in such case, as shown in Figures 13b-c, and the tail width at 95 gf was larger than those at 55 gf and 75 gf, since larger bonding force at the wedge could squeeze enough material at the heel of the bond resulting in a bond failure easily, which should not be accepted. So, the optimal ultrasonic power of 90 mW and bonding force of 75 gf were chosen here for the wedge bond of AAPPCA wire in order to ensure wedge bond quality.
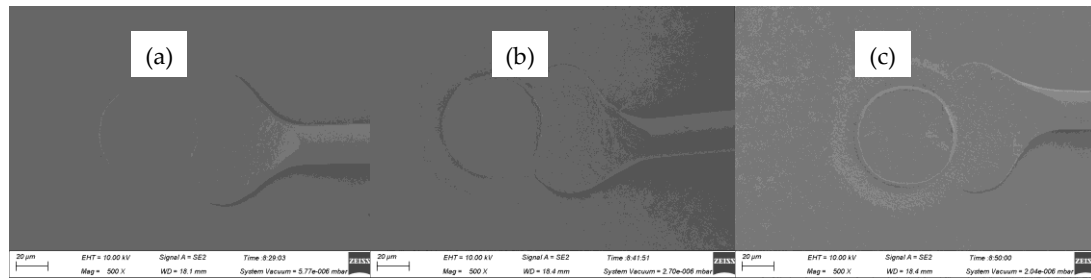
Figure 13. Wedge bond morphologies of AAPPCA wire for different ultrasonic power at 95 gf: (a) 80 mW, (b) 90 mW, (c) 100 mW

3.5. Bond Strength Test of AAPPCA wire

Destructive pull test is the most widely used technique to evaluate the bond strength by hooking and pulling the bonded wire until it fails, and the major failure modes that one observes during a bond pull test are, ball bond lift (Location A), ball neck break (Location B), midspan wire break (Location C), heel break (Location D) and wedge bond lift (Location E), as is shown in Figure 14. The test results are important evidences for certifying the proper setup of the process parameters and evaluating bonding quality and reliability. Wire break at B, C or D is the preferred break during the pull strength test, which indicates a strong bond between the wire and the metallization.
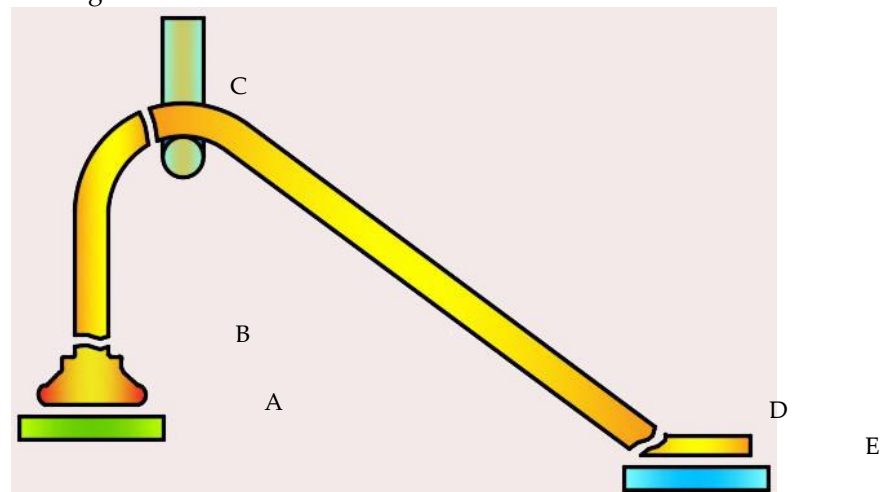

Figure 14. Pull test failure modes.

Here, twenty bonded wire samples, obtained at optimal process parameters (25 mA and 650 μs for FAB, 70 mW and 45 gf for ball bond, 90 mW and 75 gf for wedge bond), were chosen randomly to carry on the destructive pull test, and the test results were shown in Table 2, it was obvious that all the bonded wire samples break at B, C or D, no failure happened at A and D. Moreover, it could be clearly seen from Figure 15 that ball neck break is the predominant failure mode for bond wire samples, a possible reason was that there existed highest stress concentration at B, which would easily induce ball neck cracking failure. The pull force ranged from 9.6 gf to 13.4 gf, as shown in Figure 16, and the minimum value of pull force is larger than standard one [29], which meant that all bonded wire samples have high bond strength.

Table 2. Destructive pull and ball shear tests results of bonded wire samples

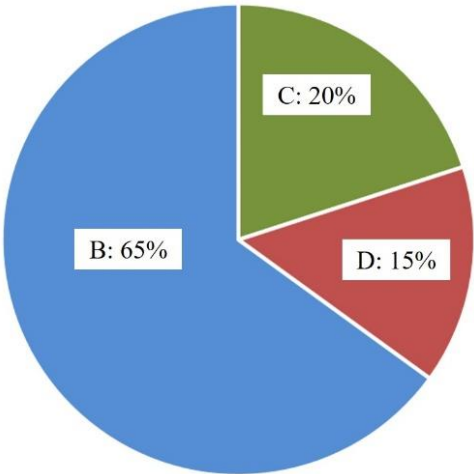| Samples	Destructive Pull Test		Ball Shear Test
	Break Location	Pull Force/gf	Shear Force/gf
1	B	12.5	40.6
2	D	10.2	42.5
3	C	12.7	39.6
4	B	9.7	38.4
5	B	11.5	34.1
6	D	13.4	41.6
7	B	12.1	45.7
8	C	11.4	38.9
9	B	10.6	33.2
10	B	9.8	42.6
11	B	12.8	43.8
12	C	11.6	39.4
13	D	11.9	41.8
14	B	12.6	42.8
15	B	9.6	49.7
16	B	11.8	33.6
17	C	12.7	40.8
18	B	12.4	38.6
19	B	11.7	45.7
20	B	11.2	44.6

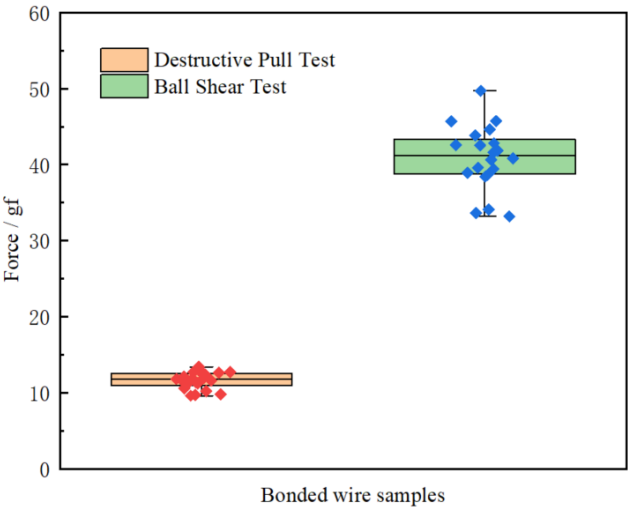**Figure 15.** Percentage diagram of break locations after destructive pull test.

Figure 16. Oneway analyses of pull and shear forces.

The destructive pull test is suitable for most applications, however it provides very little information on the ball bond strength and quality, thus it fails in determining the true ball bond strength. This factor has led to the development of ball shear test, and it is performed using a shear tool to push off ball bond with a sufficient force, as shown in Figure 17, whose results can reflect the intermetallic formation and its coverage of ball bonds. The shear force results of the twenty bonded wire samples were shown in Table 2, who ranged from 33.2 gf to 45.7 gf, as shown in Figure 16, and the minimum value of shear force is also larger than standard one [29]. Figure 18 presented a typical SEM image of ball band after sheared, full intermetallic compound (IMC) coverage with regular morphology was found on the bond pad, which enhanced the adhesion of bond to pad. The above pull and shear test results showed that the bonded wire samples have enough bond strength, and hence improve the reliability of microelectronic products.
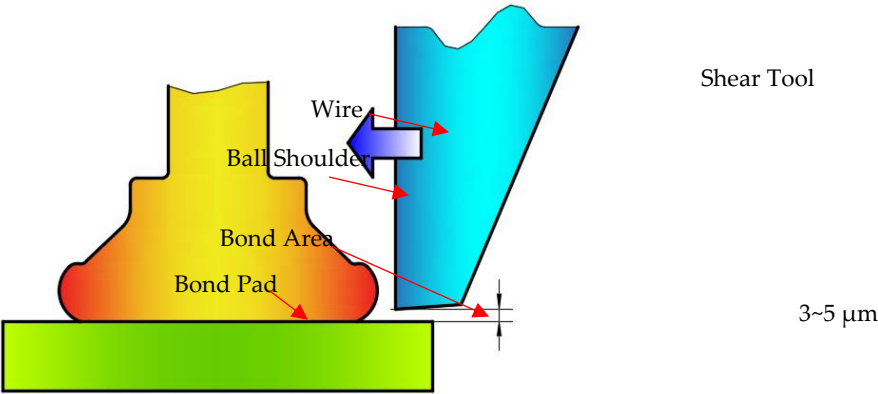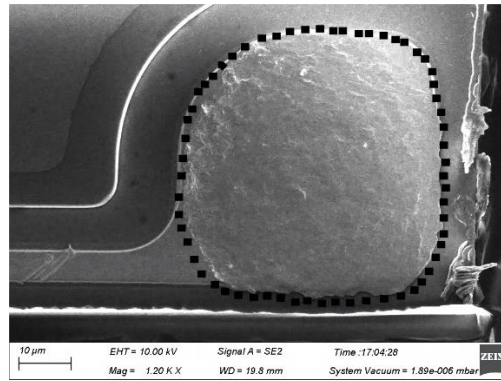

Figure 17. Ball shear test.

Figure 18. Typical ball bond morphology after ball shear test.

4. Conclusions

In our study, we have drawn the following conclusions pertaining to the effects of different process parameters on bond properties of AAPPCA Wire:

(1) As the EFO time increases from 550 µs to 750 µs, the FAB of AAPPCA Wire grows from a preheated tip to a small ball with a hollow at its bottom at 20 mA, while it changes from a small ball to a regular ball and finally to a golf ball at 25 mA. When the EFO current is 30 mA, all the FABs exhibit golf balls. The EFO current and time for a regular and smooth FAB are 25 mA and 650 µs, respectively.

(2) For the AAPPCA Wire, at a constant EFO current of 25 mA, the relationship between the FAB diameter and EFO time can be expressed by a cubic equation obtained through fitting the experimental data by using least square method.

(3) For ball bond, the mashed ball diameter of AAPPCA Wire increases with increasing either the ultrasonic power or the bonding force. For wedge bond, with the increase of ultrasonic power or bonding force, the CHI becomes more and more obvious, and the tail width increases larger and larger. The optimal ultrasonic power and bonding force are 70 mW and of 45 gf for ball bond and 90 mW and 75 gf for wedge bond, respectively.

(4) The destructive pull test results show that all the bonded wire samples obtained at optimal process parameters break at B, C or D, and full IMC coverage with regular morphology occurs on the bond pad after ball shear test. So, all the bonded wire samples have enough bond strength, which is beneficial to the reliability of microelectronic products.

References

1. Zhou H.L.; Zhang Y.C.; Cao J.; Su C.H.; Li C.; Chang A.D.; An B. Research progress on bonding wire for microelectronic packaging. *Micromachines* **2023**, *14,* 432.
2. Hamid K.A.; Badarisman A.H.; Jalar A.; Bakar M.A. Investigation of integrated factors in the occurrence of copper wire bonding corrosion of semiconductor packages. *J. Phys. Conf. Ser.* **2022**, *2169*, 12016.
3. Alim M.A.; Abdullah M.Z.; Aziz M.S.A.; Kamarudin R. Die attachment, wire bonding, and encapsulation process in LED packaging: A review. *Sensor. Actuat. A phys.* **2021**, *329*, 112817.
4. Yu C.M.; Lai K.K.; Chen K.S.; Chang T.C. Process-quality evaluation for wire bonding with multiple gold wires. *IEEE Access* **2020**, *8*, 106075-106082.
5. Mokhtari O.; Nishikawa. Effect of surface potential distribution on corrosion behavior of Cu/Al interface in Cu wire bonding applications. *Microelectron. Reliab.* **2020**, *113*, 113942.
6. Schneider-Ramelow M.; Ehrhardt C. The reliability of wire bonding using Ag and Al. *Microelectron. Reliab*. **2016**, *63*, 336-341.
7. Chuang T.H.; Lin H.J.; Chuang C.H.; Shiue Y.Y.; Shieu F.S.; Huang Y.L.; Hsu P.C.; Lee J.D.; Tsai H.H. Thermal stability of grain structure and material properties in an annealing twinned Ag–4Pd alloy wire. *J. Alloy. Compd*. **2014**, *615*, 891-898.
8. Xie Q.; Long K.; Lu D.N.; Li D.W.; Zhang Y.; Wang J. Integrated circuit gold wire bonding measurement via 3-D point cloud deep learning. *IEEE T. Ind. Electron.* **2022**, *69*, 11807-11815.
9. Xie S.; Lin P.R.; Yao Q.B. Interface mechanical behavior of gold alloy wire bonding. *J. Phys. Conf. Ser.* **2021**, *1907*, 12021.
10. He X.K.; Guo L.B.; Gong G.S.; Su F.L.; Zhu D.C. Effects of different inhibitor on antioxidation of copper bonding wire at room temperature. *J. Mater. Sci. Mater. El.* **2022**, *33,* 10561–10571.
11. Gu B.K.; Shen S.N.; Li H. Mechanism of microweld formation and breakage during Cu–Cu wire bonding investigated by molecular dynamics simulation. *Chinese phys. B* **2022**, *31*, 16101.
12. Eto M.; Araki N.; Yamada T.; Sugiyama M.; Fujimoto S. Influence of post-bonding heating process on the long-term reliability of Cu/Al contact. *Microelectron. Reliab*. **2021**, *118*, 114058.
13. Eto M.; Araki N.; Yamada T.; Sugiyama M.; Fujimoto S. Microstructural characterization of alloyed palladium coated copper wire under high temperature. *Microelectron. Reliab*. **2021**, *120,* 114125.
14. Manoharan S.; Patel C.; Mccluskey P. Advancements in Silver Wire Bonding. In Proceedings of the ASME 2017 International Technical Conference and Exhibition on Packaging and Integration of Electronic and Photonic Microsystems. San Francisco, California, USA, 29 August-1 September 2017.
15. Jhan J.J.; Wataya K.; Nishikawa H.; Chen C.M. Electrodeposition of nanocrystalline Cu for Cu-Cu direct bonding. *J. Taiwan Inst. Chem. E*. **2022**, *132*, 104127.
16. Chuang T.H.; Lee P.I.; Lin Y.C. An Optimized Ag–5Pd–3.5Au bonding wire for the resistance of Ag ion migration in LED packages. *IEEE T. Comp. Pack. Man*. **2020**, *10*, 1989-1995.
17. Xi J.Q.; Mendoza N.; Chen K.; Yang T.; Reyes E.; Bezuk S.; Lin J.; Ke S.; Chen E. Evaluation of Ag wire reliability on fine pitch wire bonding. In Proceedings of the 2015 65th Electronic Components and Technology Conference. San Diego, CA, USA, 26-29 May 2015.
18. Tanna S.; Pisigan L.J.; Song W. H.; Halmo C.; Persic J.; Mayer M. Low cost Pd coated Ag bonding wire for high quality FAB in air. In Proceedings of the 2012 IEEE 62nd Electronic Components and Technology Conference. San Diego, CA, USA, 29 May-1 June 2012.
19. Zhong M.J.; Huang F.X.; Ruan H.G.; Wu B.A.; Tang H.Y.; Luo W.F. Research progress on the copper and silver bonding wire materials. Materials Reports **2017**, *31*, 99-102.
20. Cao J.; Wu W.X. Effects of Au coated Ag bonding wire properties on bonded quality. *Mater. Sci. Tech-Lond*. **2018**, *26*, 30-35.
21. Czerny B.; Mazloum-Nejadari A.; Khatibi G.; Weiss L.; Zehetbauer M. Fatigue testing method for fine bond wires in an LQFP package. *Microelectron. Reliab.* **2016**, *64*, 270-275.
22. Liang S.; Huang F.X.; Peng C.; Zhong M.J.; Wu B.A.; Tang H.Y. Research progress on copper and silver bonding wires for microelectronic packaging technology. *J. Funct. Mater.* **2019**, *50*, 5048-5053.
23. Fan J.L.; Zhu L.X.; Cao J.; Hua H. Effects of Au component in Ag alloy bonding wire on bonded strength and bonded reliability. *J. Funct. Mater*. **2019**, *50*, 10145-10148.

24. Tsai C.H.; Chuang C.H.; Tsai H.H.; Lee J.D.; Dennis Chang D.; Lin H.J.; Chuang T.H. Materials characteristics of Ag-alloy wires and their applications in advanced packages. *IEEE T. Comp. Pack. Man*. **2016**, *6*, 298-305.
25. Cao J.; Zhang J.C.; Wu B.A.; Tang H.Y.; Lv C.C.; Song K.S.; Cui C.Q.; Gao Y.G. Study on manufacturing technology of Ag-8.5Au-3.5Pd fine alloy wire. *Micromachines* **2021**, *12*, 938.
26. Chuang T.S.; Wang H.C.; Chuang C.H.; Lee J.D.; Tsai H.H. Effect of annealing twins on electromigration in Ag-8Au-3Pd bonding wires. *J. Electron. Mater*. **2013**, *42*, 545-551.
27. Chuang T.S.; Wang H.C.; Chuang C.H.; Lee J.D.; Tsai H.H. Effects of annealing twins on the grain growth and mechanical properties of Ag-8Au-3Pd bonding wires. *J. Electron. Mater*. **2012**, *41*, 3215-3222.
28. Cao J.; Zhang J.C.; Persic J.; Song K.X. Effects of bonding parameters on free air ball properties and bonded strength of Ag-10Au-3.6Pd alloy bonding wire. *Micromachines* **2020**, *11*, 777.
29. Cao, J. Research of copper bonding wire performance and bonding performance. Doctoral Thesis, Lanzhou University of Technology, Lanzhou, June 2012.